Check for updates

A physical interpretation of coupling chiral metaatoms†

Zhaolong Cao, Jianfa Chen, Shaozhi Deng and Huanjun Chen [ID] *

The physical origins of chiroptical responses from artificial optically active media are significant for developing high-performance circular dichroism (CD) spectroscopic techniques. Here, we present a biorthogonal approach based on temporal coupled-mode theory to unravel the underlying physics of chiral metasurfaces. Equipped with physically meaningful parameters, this approach inherits the intrinsic properties of open optical cavities, including time-reversal symmetry and non-Hermitian Hamiltonians, which are found to be in excellent agreement with numerical results. Remarkably, it identifies that the intrinsic chirality of coupled chiral nanocavities arises from (i) the asymmetric coupling between interlayer cross-polarized resonant modes and (ii) a coherent interference between doubly degenerate states. Based on this formalism, a critical coupling condition capable of achieving zero transmission for circularly polarized light is proposed.

State Key Laboratory of Optoelectronic Materials and Technologies, Guangdong Province Key Laboratory of Display Material and Technology, School of Electronics and Information Technology, Sun Yat-sen University, Guangzhou 510275, China. E-mail: chenhj8@mail.sysu.edu.cn
†Electronic supplementary information (ESI) available. See DOI: 10.1039/d1nr05065f

Huanjun Chen

Dr Huanjun Chen obtained his PhD degree in physics from The Chinese University of Hong Kong in 2010. He then did his postdoctoral research there from 2010 to 2012. In January 2012, he joined the School of Physical Science and Engineering in Sun Yat-sen University as an associate professor. Currently, he is a full professor in the School of Electronics and Information Technology. Dr Chen focused on the research of low-dimensional polaritonic materials and their optoelectronic devices. In the past five years, his research activities were focused on polaritonic two-dimensional atomic crystals and their applications in terahertz and mid-infrared detection.

Introduction

A chiral object refers to a geometrical object, or a group of points, whose mirror image (enantiomer) cannot be brought to coincide with itself.[1] Although chirality is mostly associated with structural properties at its initial stage, chiral structures can manifest themselves with rich physics ranging from topological surface states[2] and chiral excitonic states[3] to enhanced optical chirality.[4] For example, the ability of chiral media that exhibit differential responses to left circularly polarized (LCP) and right circularly polarized (RCP) lights, termed circular dichroism (CD), has been widely used as a powerful analytical tool in enantiomer characterization for centuries.[5] However, the chiral-optical (chiroptical) effect is a subtle property at optical frequencies due to the weak magnetic responses of naturally occurring materials, and a medium with strong chiroptical effects is still challenging to achieve.[6–10]

Recently, artificial metasurfaces based on plasmonic nanostructures and high-index dielectric nanoparticles have emerged as a research hotspot owing to their unprecedented capabilities for manipulating and localizing photons at a subwavelength scale.[9,11,12] Various complex geometries, including split-ring resonators,[13–15] gammadions,[16–18] L- and S-shaped antennas,[19] and nanoclusters,[20–24] have been extensively studied as basic building blocks for chiral metasurfaces. Recently, giant chirality with maximum CD has been reported both theoretically[25] and experimentally.[15,17] However, the underlying physics governing the physical origins of chiroptical responses is still not well studied. For example, chiral plasmonic structures can be modeled with two mutually coupled

harmonic oscillators from an electromagnetic perspective, which has been demonstrated to not only provide an intuitive framework but also being in qualitative agreement with experimental observations.[22,26] However, this phenomenological approach, based on the coupling between resonators, is a classical analog to the constitutive relationships of optically active media.[27,28] The fundamental properties of open optical systems, including time-reversal symmetry and non-Hermitian interactions, are inevitably overlooked. In contrast, temporal coupled-mode theory (CMT),[29–33] a theoretical approach fruitfully employed to model optical cavities,[25,34] bears great potential for solving this problem. It has been shown that CMT provides superior accuracy on the reconstruction of the far field properties from the given eigenmodes.[35] However, a rigorous CMT based on the non-Hermitian interactions of optical cavities still remains unexplored. For instance, a recent CMT pre-assumes the eigenmodes of a chiral metasurface to be orthogonal and well-separated,[25,34] and the physical origins of chirality, that is, how the non-Hermitian coupling between achiral nanocavities gives rise to chiral eigenmodes has not been fully investigated. As shown in Fig. 1a, the metaatom is expected to exhibit giant optical chirality owing to the optical resonance and chiral arrangements. However, the physics behind non-Hermitian interactions among 8 identical achiral nanorods contributing to optical activity is still unclear. To the best of our knowledge, a rigorous derivation that combines both physical insights and explicit expressions including eigenfrequencies, eigenmodes, radiative decay rates, *etc.*, is still elusive.

Despite its importance, the main difficulty in applying CMT as a solid theoretical model is that it is intrinsically limited by two facts: (i) the model parameters in CMT are phenomenological quantities; and (ii) there is a lack of an intuitive but rigorous approach for obtaining non-orthogonal chiral eigenmodes. The former concern has been addressed by recent studies on the quasinormal mode (QNM) of electromagnetic systems,[35–38] where the classical CMT is found to be a special form of a rigorous QNM coupling theory for the case of weak coupling and low loss.[37] Here, we attempt to address the latter concern using a biorthogonal approach.[39] With surprisingly high accu-

racy, this approach reconstructs the far-field property of a chiral metasurface with meaningful parameters while still inheriting the necessity of optical systems including time-reversal symmetry and non-Hermitian interactions. Furthermore, we identified that the optical activity originates from the asymmetric coupling between interlayer cross-polarized resonant modes and the coherent interference between doubly degenerate states. In the end, we validate our formalisms through numerical simulations and propose a critical coupling condition capable of achieving zero transmission for circularly polarized light.

Results and discussion

Non-Hermitian Hamiltonian based on CMT

We should first comment on the symmetry of the chiral metasurface. Optical chirality is a time-even and parity-odd quantity.[4] However, when associated with a specific object, it could probably be intertwined with circular polarization conversion (CPC) and asymmetric transmission (AT).[24,40,41] For example, two-dimensional planar metasurfaces are geometrically achiral in three dimensions,[42] but they can still produce non-zero CD signals.[43,44] This phenomenon, also termed 2D chirality, is reported to have no contribution to optical activities.[45–47] In addition, CPC and AT effects could be absent in chiral materials (*e.g.*, an infinite slab of Pasteur medium), suggesting that they are not the fundamental mechanism for chirality. Therefore, in order to eliminate CPC and AT effects, the chiral metasurface can be chosen to have a D_4 symmetry (section S1 in the ESI†).[22,25,40,48–54] Fig. 1a shows an exemplary chiral metaatom. For the purpose of this study, we limited our analysis only to this configuration. CD is defined as CD = $(|t_+|^2 - |t_-|^2)/(|t_+|^2 + |t_-|^2)$, where $t_\pm$ is the transmission coefficient for RCP and LCP light, respectively. Here, each nanorod represents a plasmonic nanocavity. Their positive dipole moments are defined in Fig. 1b. We should stress that the constitutional building blocks can be extended to other nanocavities such as high-index Mie resonators,[11,55] split-ring resonators,[14] hyper-
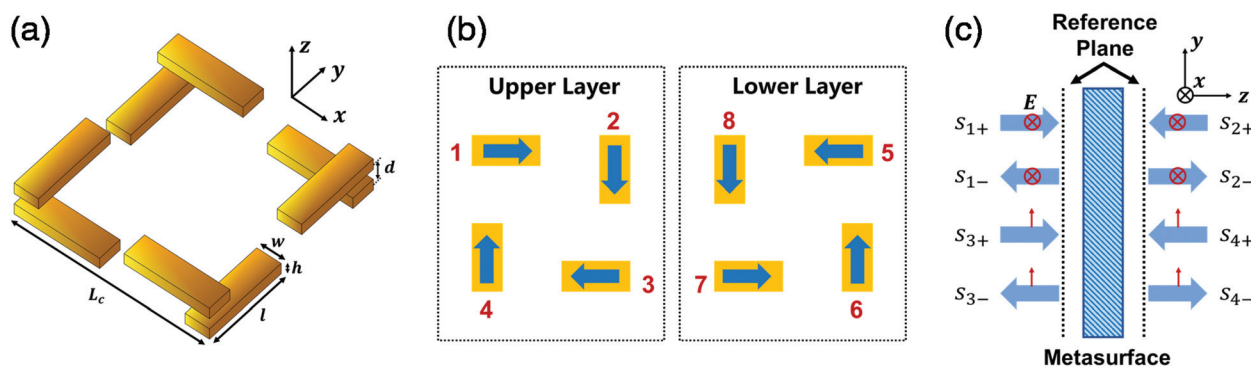

Fig. 1 Despite its importance, the main difficulty in applying CMT as a solid theoretical model is that it is intrinsically limited by two facts: (i) the model parameters in CMT are phenomenological quantities; and (ii) there is a lack of an intuitive but rigorous approach for obtaining non-orthogonal chiral eigenmodes.

bolic cavities[56] *etc.* The metaatom is embedded in a homogeneous dielectric environment. All incoming waves are incident normally to the metasurface from both sides. $e^{j\omega t}$ time dependence for all fields is assumed throughout this paper. The period is smaller than the resonant wavelength so that only zero-order transmission/reflection is allowed. In the regime of effective medium theory, this symmetry condition is a direct analog to reciprocal (Pasteur) bi-isotropic materials.[27,57]

We derive our equations based on temporal CMT.[31] As a starting point, we first denote the incoming waves by $|s_+\rangle = (s_{1+} \quad s_{2+} \quad s_{3+} \quad s_{4+})^{\mathrm{T}}$, where $s_{1+}(s_{3+})$ and $s_{2+}(s_{4+})$ are the *x*-polarized (*y*-polarized) light incident from $-z$ and $+z$ sides (Fig. 1c). Therefore, $|s_+\rangle = (1 \quad 0 \quad j \quad 0)^{\mathrm{T}}/\sqrt{2}$ and $(0 \quad 1 \quad 0 \quad -j)^{\mathrm{T}}/\sqrt{2}$ correspond to RCP incident light, and $(1 \quad 0 \quad -j \quad 0)^{\mathrm{T}}/\sqrt{2}$ and $(0 \quad 1 \quad 0 \quad j)^{\mathrm{T}}/\sqrt{2}$ correspond to LCP incident light, respectively. Similarly, the outgoing waves are defined by $|s_-\rangle = (s_{1-} \quad s_{2-} \quad s_{3-} \quad s_{4-})^{\mathrm{T}}$. The incoming and outgoing waves can couple through a direct pathway described by a background S-matrix C, which is unitary and symmetric for a lossless and reciprocal system in the absence of optical cavities. By properly choosing a reference input plane and considering symmetry requirements,[30] C takes the form (section S2 in the ESI†)

$$C = \begin{pmatrix} -\cos\xi & j\sin\xi & & \\ j\sin\xi & -\cos\xi & & \\ & & -\cos\xi & j\sin\xi \\ & & j\sin\xi & -\cos\xi \end{pmatrix} \quad (1)$$

where ξ is a real number with $-\cos\xi$ and $j\sin\xi$ being the background reflection and transmission coefficients. Once the background S-matrix, input, and output waves are defined, the dynamic equations for coupled nanocavities can be written as[31]

$$\frac{d\boldsymbol{a}}{dt} = j(\Omega + j\Gamma)\boldsymbol{a} + K^{\mathrm{T}}|s_+\rangle \quad (2.1)$$

$$|s_-\rangle = C|s_+\rangle + D\boldsymbol{a}, \quad (2.2)$$

where $\boldsymbol{a} = (a_1 \quad a_2 \quad ... \quad a_8)^{\mathrm{T}}$ represents the complex resonant amplitudes of nanocavities and $\Gamma = K^+K/2$ is the radiative coupling matrix. The excitation matrix for incoming waves is given by: $K = (\kappa_1 \quad \kappa_2 \; ... \; \kappa_8)$, where κ_i is a 4 × 1 vector representing the position-dependent radiative excitation coefficient for the ith cavity (section S3 in the ESI†). For example, the longitudinal LSPR mode for the 1st plasmonic nanorods can be defined as

$$\kappa_1 = \sqrt{\Gamma_{\mathrm{rad}}} e^{-\frac{\pi}{4}j} \begin{pmatrix} e^{-j(\phi-\frac{\pi}{4})} \\ e^{j(\phi-\frac{\pi}{4})} \\ 0 \\ 0 \end{pmatrix} \quad (3)$$

The phase factor π/4 in eqn (3) is due to the choice of the reference input plane in eqn (1). The physical interpretation of ϕ is a retardation coefficient for $+z$ and $-z$ incoming waves, which are related to the layer distance and the wavevector of incoming waves by $kd = 2(\phi - \pi/4)$. The decay matrix is defined

by $D = K$ because of time-reversal symmetry. $\Gamma_{\mathrm{rad}} = |\kappa_i|^2/2$ is the total radiative decay rate for a single cavity. The near field interactions and complex resonant frequencies of nanocavities can be represented by an 8 × 8 symmetric matrix

$$\Omega = \begin{pmatrix} \Omega_0 & \Omega_{\mathrm{c}}^{\mathrm{T}} \\ \Omega_{\mathrm{C}} & \Omega_0 \end{pmatrix} \quad (4.1)$$

where Ω_0 and Ω_{c} are 4 × 4 coupling matrices, representing intralayer and interlayer near field interactions. Bound by symmetry, Ω_0 and Ω_{C} are circulant matrices

$$\Omega_0 = \begin{pmatrix} \omega_0 + j\Gamma_{\mathrm{abs}} & \omega_{12} & -\omega_{13} & \omega_{12} \\ \omega_{12} & \omega_0 + j\Gamma_{\mathrm{abs}} & \omega_{12} & -\omega_{13} \\ -\omega_{13} & \omega_{12} & \omega_0 + j\Gamma_{\mathrm{abs}} & \omega_{12} \\ \omega_{12} & -\omega_{13} & \omega_{12} & \omega_0 + j\Gamma_{\mathrm{abs}} \end{pmatrix} \quad (4.2)$$

$$\Omega_{\mathrm{C}} = \begin{pmatrix} -\omega_{15} & -\omega_{18} & -\omega_{17} & -\omega_{16} \\ -\omega_{16} & -\omega_{15} & -\omega_{18} & -\omega_{17} \\ -\omega_{17} & -\omega_{16} & -\omega_{15} & -\omega_{18} \\ -\omega_{18} & -\omega_{17} & -\omega_{16} & -\omega_{15} \end{pmatrix} \quad (4.3)$$

where ω_0 and Γ_{abs} are the resonant frequency and absorption rate of an individual nanocavity, and ω_{12}, ω_{13}, ω_{15}, ω_{16}, ω_{17} and ω_{18} are near-field coupling coefficients among nanocavities. Note that $\omega_{14} = \omega_{12}$ due to rotational symmetry. The minus sign reflects the mutual excitation between nanocavities by considering the orientation of dipole moments (Fig. 1b).

Considering both near-field and far-field interactions, the Hamiltonian of the optical system leads to the symmetric non-Hermitian matrix: $H = \Omega + j\Gamma$. The off-diagonal (complex) elements of H correspond to the mutual excitation of the scattered fields between each nanocavity from the first principles of Maxwell's equations.[37] As we will show later, H manifests itself with rich physics by the biorthogonal approach.

Chiral eigenmodes based on the biorthogonal approach

We start with the biorthogonal approach on the non-Hermitian H matrix. Assuming that X_{R} is a matrix whose columns are the right eigenvectors of H, and X_{L} is a matrix whose rows are the left eigenvectors of H, one can obtain $X_{\mathrm{L}}^{\mathrm{T}} = X_{\mathrm{R}}$ and $X_{\mathrm{L}}X_{\mathrm{R}} \equiv 1$ (section S4 in the ESI†). Then, the general CMT equations can be reorganized by left-multiplying eqn (2.1) with X_{L}

$$\frac{d}{dt}(X_{\mathrm{L}}\boldsymbol{a}) = jH_0(X_{\mathrm{L}}\boldsymbol{a}) + X_{\mathrm{L}}K^T|S_+\rangle \quad (5.1)$$

$$|s_-\rangle = C|s_+\rangle + KX_{\mathrm{R}}(X_{\mathrm{L}}\boldsymbol{a}) \quad (5.2)$$

where H_0 is a diagonal matrix describing eigenfrequencies. Comparing eqn (2) and (5), one can find that $\boldsymbol{a}' = X_{\mathrm{L}}\boldsymbol{a}$ corresponds to the eigenmodes of the optical system. In addition, the excitation matrix for $\boldsymbol{a}'$ still follows time-reversal symmetry given by $K' = (\kappa'_1 \quad \kappa'_2 \quad \cdots \quad \kappa'_8) = (X_{\mathrm{L}}K^{\mathrm{T}})^{\mathrm{T}} = KX_{\mathrm{R}} = D'$. Note that due to the non-Hermitian nature ($X_{\mathrm{L}}^+X_{\mathrm{L}} \neq 1$), the radiative decay rate for the ith eigenmode should be normalized by $\Gamma_{\mathrm{rad},i} = |\kappa_i|^2/(2|a_i|^2)$.

Next, we attempted to deduce the explicit equation for X_L. The direct diagonalization of the 8×8 non-Hermitian matrix is a non-trivial task. However, a two-step diagonalization process, namely, intralayer and interlayer diagonalizations, can simplify the mathematical derivations. From a physical point of view, this is equivalent to categorizing cavity interactions into two groups: (i) nanocavities in the same layer first couple together (intralayer interaction) forming intralayer eigenmodes, and then (ii) couple to the opposite layer (interlayer interaction). Detailed derivations are given in section S5 of the ESI,† and we only list several physical implications here.

First, by performing intralayer diagonalization and reorganization, one obtains the block-diagonal Hamiltonian

$$
H_2 = \begin{pmatrix}
\tilde{\omega}_1 & \tilde{\omega}_{15} & & & & & & \\
\tilde{\omega}_{15} & \tilde{\omega}_1 & & & & & & \\
& & \tilde{\omega}_2 & \tilde{\omega}_{26} & & & & \\
& & \tilde{\omega}_{26} & \tilde{\omega}_2 & & & & \\
& & & & \tilde{\omega}_3 & & \tilde{\omega}_{37} & \tilde{\omega}_{38} \\
& & & & & \tilde{\omega}_3 & -\tilde{\omega}_{38} & \tilde{\omega}_{37} \\
& & & & \tilde{\omega}_{37} & -\tilde{\omega}_{38} & \tilde{\omega}_3 & \\
& & & & \tilde{\omega}_{38} & \tilde{\omega}_{37} & & \tilde{\omega}_3
\end{pmatrix}
\tag{6}
$$

where $\tilde{\omega}_1 = \omega_0 - 2\omega_{12} - \omega_{13} + j\Gamma_{\text{abs}}$, $\tilde{\omega}_2 = \omega_0 + 2\omega_{12} - \omega_{13} + j\Gamma_{\text{abs}}$, and $\tilde{\omega}_3 = \omega_0 + \omega_{13} + 2j\Gamma_{\text{rad}} + j\Gamma_{\text{abs}}$ are the intralayer eigenfrequencies, and $\tilde{\omega}_{15} = -\omega_{15} + \omega_{16} - \omega_{17} + \omega_{18}$, $\tilde{\omega}_{26} = -\omega_{15} - \omega_{16} - \omega_{17} - \omega_{18}$, $\tilde{\omega}_{37} = -\omega_{15} + \omega_{17} - 2j\Gamma_{\text{rad}} \sin 2\phi$, and $\tilde{\omega}_{38} = \omega_{16} - \omega_{18}$ are the interlayer coupling coefficients. Therefore, the interlayer interaction can be divided into three diagonal block parts. While the first two blocks are total dark modes owing to the C_4 rotational symmetry (section S5 in the ESI†), radiative modes from

$$
H_3 = \begin{pmatrix}
\tilde{\omega}_3 & & \tilde{\omega}_{37} & \tilde{\omega}_{38} \\
& \tilde{\omega}_3 & -\tilde{\omega}_{38} & \tilde{\omega}_{37} \\
\tilde{\omega}_{37} & -\tilde{\omega}_{38} & \tilde{\omega}_3 & \\
\tilde{\omega}_{38} & \tilde{\omega}_{37} & & \tilde{\omega}_3
\end{pmatrix}
$$

will contribute to chirality.

Second, the eigenmodes of H_3 are doubly degenerate. This property is of particular importance for the chiral metasurface. To understand this, we start with the explicit expression of the outgoing wave $|s_-\rangle$ (section S6 in the ESI†)

$$
|s_-\rangle = S|s_+\rangle = \begin{pmatrix}
\alpha & \beta & & \gamma \\
\beta & \alpha & -\gamma & \\
& -\gamma & \alpha & \beta \\
\gamma & & \beta & \alpha
\end{pmatrix} |s_+\rangle
\tag{7}
$$

where α, β, and γ are frequency-dependent scattering coefficients. The S-matrix in eqn (7) takes the characteristic features for the bi-isotropic(chiral) material (eqn (S8)†). As discussed in section S7 of the ESI,† this type of chirality is strictly prohibited for a single resonator due to the time-reversal constraint. That is, an isolated resonator is insufficient to construct a chiral metasurface analogue to the Pasteur medium, and chiroptical responses from a non-degenerate state will inevitably

be intertwined with the CPC or the AT effect. In contrast, for doubly degenerate systems with the same complex eigenfrequency but rotated excitation coefficients, their radiation interferes coherently giving rise to chirality (eqn (S33)†).

Third, the chiroptical response of the metasurface can be determined once the S-matrix is ready. The reflection coefficients for LCP (r_-) and RCP (r_+) lights are identical given by $r_\pm = \alpha$, whereas the transmission coefficients are $t_\pm = \beta \mp j\gamma$ (eqn (S29)†). Therefore, according to eqn (S28.4),† γ (more specifically, the product between $\tilde{\omega}_{38}$ and $\cos 2\phi$) accounts for the CD responses. Apparently, $\tilde{\omega}_{38} = \omega_{16} - \omega_{18}$ depicted in Fig. 2a is attributed to structural chirality—the asymmetric coupling from a_6 and a_8 to the cross-polarized a_1 nanocavity. When the metaatom restores to symmetry configurations (Fig. 2a, right), a_6 and a_8 cancel each other, leading to negligible chirality. ϕ corresponds to the retardation effect (eqn (3)) and will be discussed later.

Using eqn (S28.3) and (S28.4)† and assuming negligible background reflection for subwavelength nanorods ($\xi = \pi/2$), $t_\pm$ can be simplified as

$$
t_\pm = j + 2\Gamma_{\text{rad}} \left(\frac{-1 - \sin(2\phi \pm \zeta)}{(\omega - \omega_-)} + \frac{-1 + \sin(2\phi \pm \zeta)}{(\omega - \omega_+)} \right)
\tag{8}
$$

where ζ is a complex number given by $\sin \zeta = \tilde{\omega}_{38}/\sqrt{\tilde{\omega}_{37}^2 + \tilde{\omega}_{38}^2}$ and $\cos \zeta = \tilde{\omega}_{37}/\sqrt{\tilde{\omega}_{37}^2 + \tilde{\omega}_{38}^2}$. Eqn (8) is consistent with previous results.[25,34] Moreover, this formalism explicitly recovers the far-field amplitude and phase information of the system, which is crucial for explaining asymmetric chiral Fano line-shapes. Fig. 2b–d show the chiroptical behavior of an analytical metasurface with $\omega_0 + \omega_{13} = 1$, $\Gamma_{\text{rad}} = 0.005$, $\Gamma_{\text{abs}} = 0.003$, $-\omega_{15} + \omega_{17} = -0.022$, $\omega_{16} - \omega_{18} = -0.017$ and $\phi = 1.5$ rad. As expected, transmission spectra for both LCP and RCP lights exhibit Fano line-shapes (Fig. 2b) and the CD response yields characteristic bisignate signatures.

It is also noteworthy that eqn (8) predicts an isolated chiral state by evaluating the numerator

$$
-1 - \sin(2\phi \pm \zeta) = 0
\tag{9.1}
$$

or

$$
-1 + \sin(2\phi \pm \zeta) = 0.
\tag{9.2}
$$

The above equations require that, given $\tilde{\omega}_{38}$ a real coefficient, ζ, or equivalently, $\tilde{\omega}_{37}$ should be a real number as well. Therefore, recalling that $\Im(\tilde{\omega}_{37}) = -2\Gamma_{\text{rad}} \sin 2\phi = 0$, one gets $2\phi = n\pi$ for all positive integers n. For the lowest order $\phi = \pi/2$ we arrive at the assessment given by the plasmonic Born–Kuhn model:[22] the isolated chiral mode is located at a quarter-wavelength layer distance ($d = \pi/2k = \lambda/4$). In fact, such a condition is not sufficient. By inserting $\phi = \pi/2$ into eqn (9.1) and (9.2), one arrives at $\sin \zeta = \pm 1$ and thus $\Re(\tilde{\omega}_{37}) = -\omega_{15} + \omega_{17} = 0$. Therefore, isolated chiral states can only be achieved when differential near field interactions from a_5 and a_7 to the parallel a_1 nanocavity cancel each other. Considering the asymmetry positions of a_5 and a_7, this condition is difficult to be fulfilled. Nevertheless, Fig. 2e and f
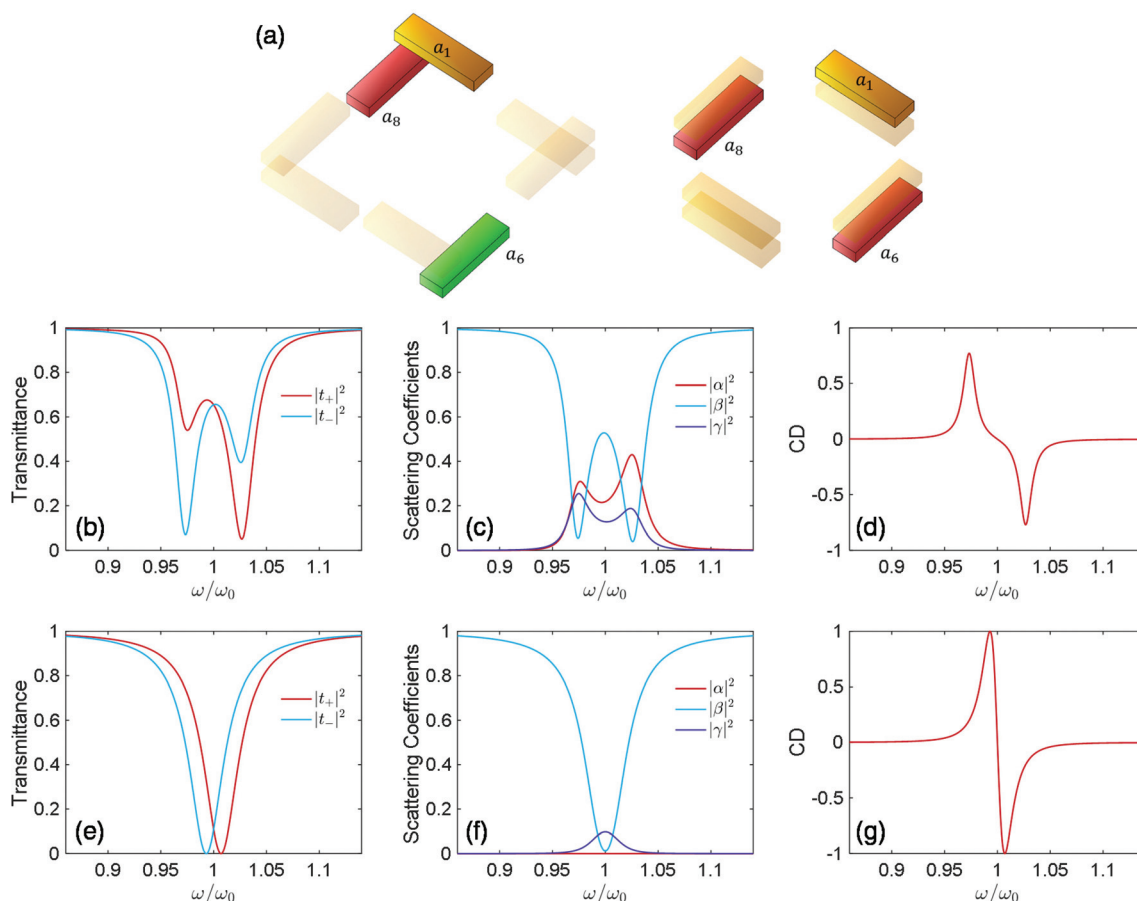
Fig. 2 Physical origins of the chiroptical response from a chiral metasurface. (a) Left: chiral coupling arises from the asymmetric coupling among a_6 and a_8 to the cross-polarized a_1 nanocavity. Right: for the achiral configuration, ω_{16} and ω_{18} cancel each other, leading to vanished $\tilde{\omega}_{38}$. (b–d) Simulated transmission (b), scattering coefficients (c), and CD (d) with $\omega_0 + \omega_{13} = 1$, $\Gamma_{\text{rad}} = 0.005$, $\Gamma_{\text{abs}} = 0.003$, $-\omega_{15} + \omega_{17} = -0.022$, $\omega_{16} - \omega_{18} = -0.017$ and $\phi = 1.5$ rad. (e–g) Isolated chiral states of transmission (e), scattering coefficients (f), and CD (g) was achieved with $\omega_0 + \omega_{13} = 1$, $\Gamma_{\text{rad}} = 0.005$, $\Gamma_{\text{abs}} = 0.01$, $-\omega_{15} + \omega_{17} = 0$, $\omega_{16} - \omega_{18} = -0.007$ and $\phi = \pi/2$.

show the analytically isolated chiral condition by setting $\omega_0 + \omega_{13} = 1$, $\Gamma_{\text{rad}} = 0.005$, $\Gamma_{\text{abs}} = 0.01$, $-\omega_{15} + \omega_{17} = 0$, $\omega_{16} - \omega_{18} = -0.007$ and $\phi = \pi/2$. Consistent with the analysis, both $|t_+|^2$ and $|t_-|^2$ exhibit a single resonant dip and demonstrate that the metaatom resonates coherently in a single state for both LCP and RCP incoming waves.

Numerical evaluations

We carried out finite-difference time-domain simulations (Lumerical Inc.) to verify the validity of chiral CMT. The geometrical parameters for the metasurface are length $l = 120$ nm, height $h = 24$ nm, width $w = 24$ nm, and atom size $L_c = 200$ nm. The metaatom is arranged in a square lattice with a period $P = 400$ nm. The permittivity of gold is best fitted from the literature[58] using the Drude model. In order to reproduce experimental conditions, the metasurface was embedded in a uniform dielectric environment with a refractive index $n = 1.5$.[22] The S-matrix was calculated using the built-in near field to far-field algorithms, and the phase of background reflection was calibrated to π according to eqn (1).

We varied the layer distance from 40 to 180 nm to facilitate different interlayer coupling strengths. Fig. 3a–c selectively show $|t_+|^2$, $|t_-|^2$ and CD spectra for strong ($d = 40$ nm), weak ($d = 60$ nm), and negligible ($d = 140$ nm) interlayer interactions. As expected, $|t_+|^2$ and $|t_-|^2$ for $d = 40$ nm exhibit two distinct resonant dips, whereas the metasurface with a distance $d = 60$ nm gives rise to Fano line-shapes. Moreover, the chiral response vanishes for $d = 140$ nm, leading to negligible CD signals. We fitted the scattering coefficients using eqn (S28)† and the results for the $d = 60$ nm metasurface are plotted in Fig. 3d–f (full fitting results can be found in section S8 of the ESI†). As one can see, eqn (S28)† recovers both the amplitude and phase information of the scattering coefficient with high accuracy.

We should comment that, despite the large amounts of independent parameters initially introduced in the CMT, only 7 coefficients, namely, $\omega_0 + \omega_{13}$, $-\omega_{15} + \omega_{17}$, $\omega_{16} - \omega_{18}$, Γ_{rad}, Γ_{abs}, ϕ, and ξ appear in the final equations. As a result, the direct fitting over 6 S-matrix spectra (real and imaginary parts of α, β, and γ) is sufficient to avoid overfitting. In addition,
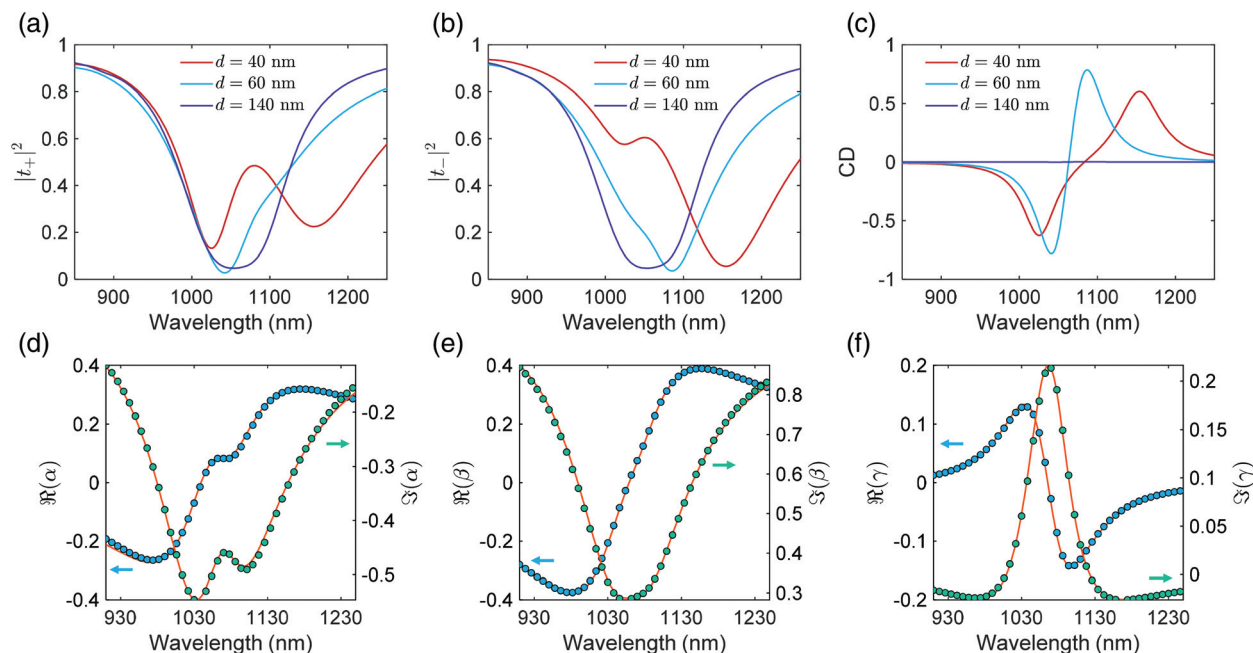
Fig. 3 Numerically simulated and fitting results for the chiral metasurface. Simulated $|t_+|^2$ (a), $|t_-|^2$ (b) and CD (c) spectra for the l = 120 nm, height h = 24 nm, width w = 24 nm, atom size L_c = 200 nm, and period P = 400 nm metasurface with layer distances of d = 40, 60, and 140 nm. The meta-surface was embedded in an n = 1.5 dielectric environment. (d–f) Fitting results (solid line) of α, β and γ for the d = 60 nm metasurface. The chiral CMT fits remarkably well with numerical simulations (circle).

these parameters all provide insightful physical meanings, which can be further used to check the validity of CMT. For example, ϕ corresponds to the retardation strength within the metasurface (eqn (S15.3)†), whereas $\Im(\tilde{\omega}_{37})$ depicts the far-field interaction (eqn (S19.9)†). Their results are confirmed by Fig. 4a and b, where the fitted and analytical calculations yield almost identical values. In addition, Γ_{abs} is the non-radiative decay rate owing to the Ohmic loss of metallic nanorods.[59] Therefore, if one keeps all geometrical parameters fixed but artificially reduces Drude's damping rates of gold for simulation, the resulting Γ_{abs} will be proportionally decreased as well.[32,36] To elucidate this, we simulated the scattering coefficients for the d = 60 nm metasurface with 70%, 30% and 0 Drude's damping rates of its original value, and compared them with analytical CMT predictions using model parameters fitted from the full loss case. As one can see from Fig. S2† (section S9 in the ESI†), CMT predictions were found to be in excellent agreement with far-field spectra, unambiguously confirming the applicability of chiral CMT. Finally, we evaluated the near field coupling coefficient $\Re(\tilde{\omega}_{37}) = -\omega_{15} + \omega_{17}$ and $\tilde{\omega}_{38} = \omega_{16} - \omega_{18}$. The interaction between subwavelength nanorods can be directly calculated from the field overlapping integral among nanocavities, which is defined as,[37,60]

$$h_{\tau,\nu} = -\omega \int_{V_\tau} \tilde{\boldsymbol{E}}_\tau \cdot \Delta\varepsilon_\tau(\boldsymbol{r},\omega) \cdot \tilde{\boldsymbol{E}}_\nu \mathrm{d}V \qquad (10)$$

where $h_{\tau,\nu}$ is the matrix element in the non-Hermitian H matrix, $\tilde{\boldsymbol{E}}_\tau$ and $\tilde{\boldsymbol{E}}_\nu$ are the QNM for τ^{th} and ν^{th} cavities, $\Delta\varepsilon_\tau = \varepsilon_\tau - \varepsilon_b$ is the permittivity difference of the τth cavity, and ε_b is

the background permittivity. Therefore, $\Re(\tilde{\omega}_{37}) = -h_{15} + h_{17} + 2j\Gamma_{rad}\sin 2\phi$ and $\tilde{\omega}_{38} = h_{16} - h_{18}$. Fig. 4c and d show the calculated near field coupling coefficient based on eqn (10). Their fitted counterparts are also superimposed for comparison. The values of both $\Re(\tilde{\omega}_{37})$ and $\tilde{\omega}_{38}$ decrease with increasing layer distance. As expected, coefficients deduced from eqn (10) corroborate with the fitted values very well, again confirming the validity of the chiral CMT. We should stress that, although CMT is well-accepted as a phenomenological model, recent developments in the QNM have unveiled its solid physical foundations, where the parameters in CMT can be directly deduced from QNM information.[36,60–67]

An important implication of the foregoing analysis is the rational design of zero transmission points for circularly polarized light. Generally speaking, the optimal CD response, defined by CD = ±1, corresponds to the zero transmission point upon either LCP or RCP excitation. Solving $t_\pm = 0$ from eqn (S24) and (S25),† one arrives at

$$\frac{1}{2}\left(\sqrt{\left((\omega_{15}-\omega_{17})^2+\tilde{\omega}_{38}^2 - 4\Gamma_{rad}^2\cos^2 2\phi\right)^2 + 16\Gamma_{rad}^2\tilde{\omega}_{38}^2\cos^2 2\phi} \right.$$
$$\left. -\left((\omega_{15}-\omega_{17})^2+\tilde{\omega}_{38}^2 - 4\Gamma_{rad}^2\cos^2 2\phi\right)\right) = \Gamma_{abs}^2.$$

$$(11)$$

Eqn (11) represents the critical coupling condition for the chiral metasurface, where the absorption rate is balanced with the function of radiative and coupling coefficients. Recalling the radiative decay rate given by $\Gamma'_{rad,i} = |\kappa'_i|^2/(2|a'_i|^2)$, Eqn (11) deviates from the classical critical coupling condition of an individual resonator.[32,33,68] In fact, this formalism is a natural
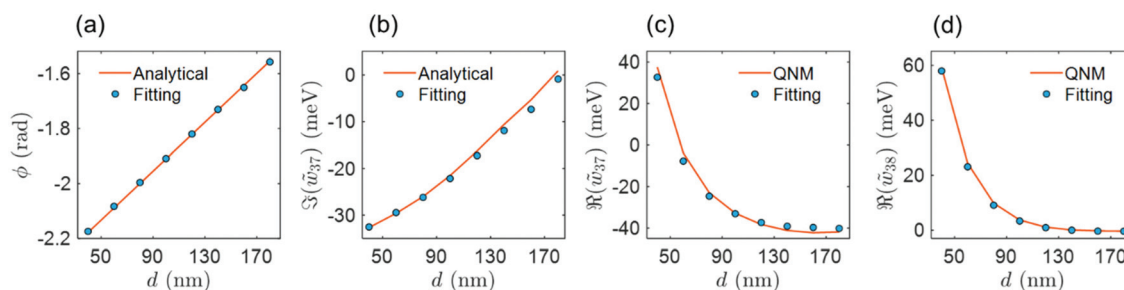
Fig. 4 Comparison between fitting parameters and analytical results. Analytical ϕ (a) and $\Im(\tilde{\omega}_{37})$ (b) from eqn (S15.3) and (S19.9)† are found to be almost identical to their fitted counterparts. In addition, the near field coupling coefficients deduced from the QNM field overlapping integral coincide well with $\Re(\tilde{\omega}_{37})$ (c) and $\tilde{\omega}_{38}$ (d).

consequence of Fano resonances and is of particular importance for coupled systems. As mode coupling is frequently exploited in designing high-performing metasurfaces, we envision that eqn (11) and the biorthogonal approach can serve as a guideline for designing non-Hermitian optical systems. For example, the absorption rate was calculated to be Γ_{abs} = 10.9 meV by using fitting parameters from the d = 40 nm metasurface, which is approximately 37.25% of intrinsic gold nanorods. We proceeded to verify eqn (11) by simulating the same metasurface with a reduced gold collision rate. As shown in Fig. 5a and b, transmission dips for both $|t_+|^2$ and $|t_-|^2$ spectra reached zero, and the corresponding CD signal increased from

0.63 to unity (Fig. 5c). Note that under this condition, the total radiative decay rates for chiral eigenmodes were deduced to be $\Gamma_{rad,+}$ = 52.5 meV and $\Gamma_{rad,-}$ = 17.4 meV. The classical critical coupling condition is not valid for Fano resonances.

As a proof of concept, we proceeded to design a practically chiral metasurface with zero transmission. The nonradiative dissipation rate calculated from Fig. 5c is about one-third of gold, which just coincides with silver nanorods. Assuming that the nonradiative decay rate depends primarily on the metal type and resonant frequency, it is expected to vary slowly with the geometry. Eqn (11) can be fulfilled by scanning the size of silver nanorods. Fig. 5d–f show the $|t_+|^2$, $|t_-|^2$ and CD response
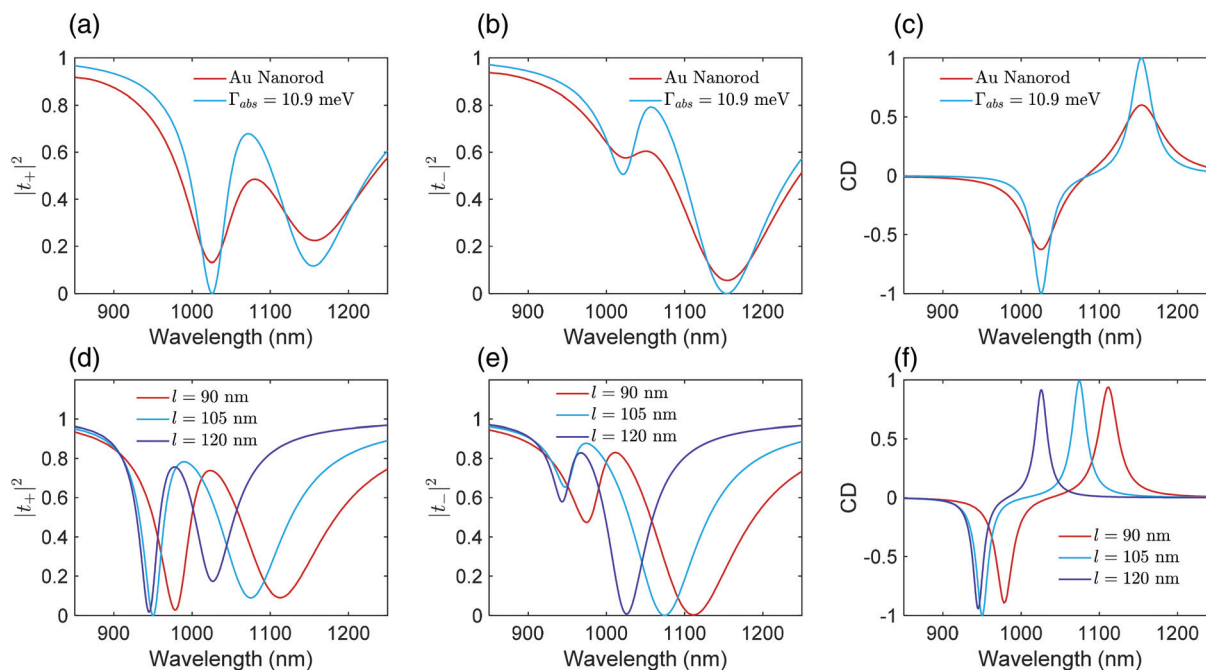
Fig. 5 Critical coupling conditions for the zero transmission condition. Transmission dips for both (a) $|t_+|^2$ and (b) $|t_-|^2$ spectra reached zero by reducing the absorption rate of the gold nanorod to Γ_{abs} = 10.9 meV. As a result, the corresponding CD (c) increased from 0.63 to unity. (d–f) A practical silver chiral metasurface with a layer distance of d = 40 nm and an atom size of L_c = 200 nm. The rod length is scanned from l = 90 to 120 nm and the aspect ratio is kept fixed $l/h = l/w = 5$. The Drude permittivity used for silver is given by $\varepsilon_{Ag} = \varepsilon_\infty + \omega_p^2/\omega(\omega - j\gamma)$, with ε_∞ = 3.7, ω_p = 1.39 × 10^{16} rad s^{-1} and γ = 3.22581 × 10^{16} rad s^{-1}. For the l = 105 nm metasurface, the fitting parameters are: $\varepsilon_0 + \omega_{13}$ = 1.2301 eV, $-\varepsilon_{15} + \omega_{17}$ = 47.6 meV, $\varepsilon_{16} + \omega_{18}$ = 58.3 meV, Γ_{rad} = 14.3 meV, Γ_{abs} = 8.6 meV, ϕ = 2.16 rad, and ξ = 1.60 rad. The deduced Γ_{abs} from eqn (10) is 8.5 meV. Note that $\Gamma_{rad,+}$ = 45.9 meV and $\Gamma_{rad,-}$ = 11.3 meV, which are also different from classical critical coupling predictions.

for the silver metasurface with different rod sizes. As expected, the zero transmission condition was achieved for length $l = 105$ nm, height $h = 21$ nm, width $w = 21$ nm, layer distance $d = 40$ nm, atom size $L_c = 200$ nm and period $P = 400$ nm.

Conclusion

In conclusion, we have proposed a generalized CMT capable of providing physical origins of chirality for coupled nanocavities. Using the biorthogonal approach, chiral CMT takes full considerations of coupled nanocavities, including non-Hermitian Hamiltonian, time-reversal symmetry, background scattering effects, physically meaningful coefficients, and geometrical symmetries. Remarkably, the closed-form expressions are found to be in excellent agreement with numerical observations. We have shown that the giant chiroptical response of a chiral metasurface is attributed to the asymmetric interlayer coupling between a_6 and a_8 to the a_1 nanocavities and the coherent interference between doubly degenerate states. In addition, the near field coupling coefficient was demonstrated to be the QNM's field overlapping between adjacent nanocavities, which can be fine-tuned by geometry parameters and constitutional materials. As a result, the CMT approach in this study can be easily transferred to other cavity systems once (i) the mode information of the isolated constitutional cavity and (ii) coupling strength between cavities are known. As both conditions have explicit formalisms (*e.g.*, eqn (2), (3) and (10)), we envision that CMT and this biorthogonal approach can serve as a guideline for designing novel non-Hermitian optical systems.

Conflicts of interest

There are no conflicts to declare.

Author contributions

Z. C., H. C., and S. D. conceived the study. Z. C. developed the theoretical model. Z. C. and J. C. performed numerical simulations. Z. C., H. C., and S. D. participated in the discussion of the data. Z. C., H. C., and S. D. supervised the project and co-wrote the manuscript with the input of all authors.

Acknowledgements

References

1 W. T. B. Kelvin, *Baltimore Lectures on Molecular Dynamics and the Wave Theory of Light*, Cambridge University Press, London, UK, 1904.

2 P. Roushan, J. Seo, C. V. Parker, Y. S. Hor, D. Hsieh, D. Qian, A. Richardella, M. Z. Hasan, R. J. Cava and A. Yazdani, *Nature*, 2009, **460**, 1106–1109.

3 Z. R. Gong, W. Z. Luo, Z. F. Jiang and H. C. Fu, *Sci. Rep.*, 2017, **7**, 42390.

4 Y. Tang and A. E. Cohen, *Phys. Rev. Lett.*, 2010, **104**, 163901.

5 B. Nina, N. Koji and R. W. Woody, *Circular Dichroism: Principles and Applications*, John Wiley & Sons, Weinheim, Germany, 2nd edn, 2000.

6 Y. Luo, C. Chi, M. Jiang, R. Li, S. Zu, Y. Li and Z. Fang, *Adv. Opt. Mater.*, 2017, **5**, 1700040.

7 Z. Hu, D. Meng, F. Lin, X. Zhu, Z. Fang and X. Wu, *Adv. Opt. Mater.*, 2019, **7**, 1801590.

8 S. Zu, T. Han, M. Jiang, F. Lin, X. Zhu and Z. Fang, *ACS Nano*, 2018, **12**, 3908–3916.

9 Z. Cao, H. Gao, M. Qiu, W. Jin, S. Deng, K.-Y. Wong and D. Lei, *Adv. Mater.*, 2020, **32**, 1907151.

10 J. T. Collins, C. Kuppe, D. C. Hooper, C. Sibilia, M. Centini and V. K. Valev, *Adv. Opt. Mater.*, 2017, **5**, 1700182.

11 K. Koshelev and Y. Kivshar, *ACS Photonics*, 2020, **8**, 102–112.

12 F. Monticone and A. Alù, *J. Mater. Chem. C*, 2014, **2**, 9059–9072.

13 D. R. Smith, J. B. Pendry and M. C. Wiltshire, *Science*, 2004, **305**, 788–792.

14 X. Xiong, W.-H. Sun, Y.-J. Bao, M. Wang, R.-W. Peng, C. Sun, X. Lu, J. Shao, Z.-F. Li and N.-B. Ming, *Phys. Rev. B*, 2010, **81**, 075119.

15 S. Yang, Z. Liu, S. Hu, A. Z. Jin, H. Yang, S. Zhang, J. Li and C. Gu, *Nano Lett.*, 2019, **19**, 3432–3439.

16 E. Hendry, T. Carpy, J. Johnston, M. Popland, R. V. Mikhaylovskiy, A. J. Lapthorn, S. M. Kelly, L. D. Barron, N. Gadegaard and M. Kadodwala, *Nat. Nanotechnol.*, 2010, **5**, 783–787.

17 A. Y. Zhu, W. T. Chen, A. Zaidi, Y. W. Huang, M. Khorasaninejad, V. Sanjeev, C. W. Qiu and F. Capasso, *Light: Sci. Appl.*, 2018, **7**, 17158.

18 M. Kuwata-Gonokami, N. Saito, Y. Ino, M. Kauranen, K. Jefimovs, T. Vallius, J. Turunen and Y. Svirko, *Phys. Rev. Lett.*, 2005, **95**, 227401.

19 T. Narushima, S. Hashiyada and H. Okamoto, *ACS Photonics*, 2014, **1**, 732–738.

20 C. Menzel, C. Helgert, C. Rockstuhl, E. B. Kley, A. Tunnermann, T. Pertsch and F. Lederer, *Phys. Rev. Lett.*, 2010, **104**, 253902.

21 P. Banzer, P. Wozniak, U. Mick, I. De Leon and R. W. Boyd, *Nat. Commun.*, 2016, **7**, 13117.

22 X. Yin, M. Schaferling, B. Metzger and H. Giessen, *Nano Lett.*, 2013, **13**, 6238–6243.

23 M. Hentschel, M. Schaferling, B. Metzger and H. Giessen, *Nano Lett.*, 2013, **13**, 600–606.

24 M. Hentschel, M. Schaferling, T. Weiss, N. Liu and H. Giessen, *Nano Lett.*, 2012, **12**, 2542–2547.

25 M. V. Gorkunov, A. A. Antonov and Y. S. Kivshar, *Phys. Rev. Lett.*, 2020, **125**, 093903.

26 M. S. Davis, W. Zhu, J. K. Lee, H. J. Lezec and A. Agrawal, *Sci. Adv.*, 2019, **5**, eaav8262.

27 I. V. Lindell, A. H. Sihvola, S. A. Tretyakov and A. J. Viitanen, *Electromagnetic Waves in Chiral and Bi-Isotropic Media*, Artech House, London, 1994.

28 A. Lakhtakia, V. K. Varadan and V. V. Varadan, *Time-Harmonic Electromagnetic Fields in Chiral Media, Lecture Notes in Physics*, Springer-Verlag, 1989.

29 S. Fan, W. Suh and J. D. Joannopoulos, *J. Opt. Soc. Am. A*, 2003, **20**, 569–572.

30 H. A. Haus, *Waves And Fields In Optoelectronics*, Prentice-Hall, Englewood Cliffs, N.J., 1984.

31 W. Suh, Z. Wang and S. H. Fan, *IEEE J. Quantum Electron.*, 2004, **40**, 1511–1518.

32 Z. Cao, H. Y. Lo and H. C. Ong, *Opt. Lett.*, 2012, **37**, 5166–5168.

33 Z. L. Cao, S. L. Wong, S. Y. Wu, H. P. Ho and H. C. Ong, *Appl. Phys. Lett.*, 2014, **104**, 171116.

34 A. V. Kondratov, M. V. Gorkunov, A. N. Darinskii, R. V. Gainutdinov, O. Y. Rogov, A. A. Ezhov and V. V. Artemov, *Phys. Rev. B*, 2016, **93**, 195418.

35 F. Alpeggiani, N. Parappurath, E. Verhagen and L. Kuipers, *Phys. Rev. X*, 2017, **7**, 021035.

36 W. Yan, R. Faggiani and P. Lalanne, *Phys. Rev. B*, 2018, **97**, 205422.

37 C. Tao, J. Zhu, Y. Zhong and H. Liu, *Phys. Rev. B*, 2020, **102**, 045430.

38 P. Lalanne, W. Yan, K. Vynck, C. Sauvan and J.-P. Hugonin, *Laser Photonics Rev.*, 2018, **12**, 1700113.

39 N. Moiseyev, *Non-Hermitian Quantum Mechanics*, Cambridge University Press, 2011.

40 M. Decker, R. Zhao, C. M. Soukoulis, S. Linden and M. Wegener, *Opt. Lett.*, 2010, **35**, 1593–1595.

41 V. A. Fedotov, P. L. Mladyonov, S. L. Prosvirnin, A. V. Rogacheva, Y. Chen and N. I. Zheludev, *Phys. Rev. Lett.*, 2006, **97**, 167401.

42 M. Schäferling, *Chiral Nanophotonics*, Springer, 2017.

43 B. Semnani, J. Flannery, R. Al Maruf and M. Bajcsy, *Light: Sci. Appl.*, 2020, **9**, 23.

44 R. Knipper, T. G. Mayerhofer, V. Kopecky, U. Huebner and J. Popp, *ACS Photonics*, 2018, **5**, 1176–1180.

45 J. Mun, M. Kim, Y. Yang, T. Badloe, J. Ni, Y. Chen, C.-W. Qiu and J. Rho, *Light: Sci. Appl.*, 2020, **9**, 139.

46 O. Arteaga, J. Sancho-Parramon, S. Nichols, B. M. Maoz, A. Canillas, S. Bosch, G. Markovich and B. Kahr, *Opt. Express*, 2016, **24**, 2242–2252.

47 J. Sachs, J.-P. Günther, A. G. Mark and P. Fischer, *Nat. Commun.*, 2020, **11**, 4513.

48 C. Menzel, C. Rockstuhl and F. Lederer, *Phys. Rev. A*, 2010, **82**, 053811.

49 M. Mutlu and E. Ozbay, *Appl. Phys. Lett.*, 2012, **100**, 051909.

50 D. Zarifi, M. Soleimani and A. Abdolali, *Phys. Rev. E: Stat., Nonlinear, Soft Matter Phys.*, 2013, **88**, 023204.

51 J. Kaschke, J. K. Gansel and M. Wegener, *Opt. Express*, 2012, **20**, 26012–26020.

52 S.-D. Liu, J.-Y. Liu, Z. Cao, J.-L. Fan and D. Lei, *Nanophotonics*, 2020, **9**, 3419–3434.

53 Y. Ye and S. He, *Appl. Phys. Lett.*, 2010, **96**, 203501.

54 B. Bai, K. Ventola, J. Tervo and Y. Zhang, *Phys. Rev. A*, 2012, **85**, 053808.

55 R. Verre, D. G. Baranov, B. Munkhbat, J. Cuadra, M. Käll and T. Shegai, *Nat. Nanotechnol.*, 2019, **14**, 679–683.

56 Z. Zheng, N. Xu, S. L. Oscurato, M. Tamagnone, F. Sun, Y. Jiang, Y. Ke, J. Chen, W. Huang, W. L. Wilson, A. Ambrosio, S. Deng and H. Chen, *Sci. Adv.*, 2019, **5**, eaav8690.

57 R. Zhao, T. Koschny and C. M. Soukoulis, *Opt. Express*, 2010, **18**, 14553–14567.

58 P. B. Johnson and R. W. Christy, *Phys. Rev. B: Solid State*, 1972, **6**, 4370–4379.

59 R. E. Hamam, A. Karalis, J. D. Joannopoulos and M. Soljacic, *Phys. Rev. A*, 2007, **75**, 053801.

60 B. Vial and Y. Hao, *J. Opt.*, 2016, **18**, 115004.

61 W. Chen, Q. Yang, Y. Chen and W. Liu, *Phys. Rev. Lett.*, 2021, **126**, 253901.

62 P. T. Kristensen, J. R. d. Lasson, M. Heuck, N. Gregersen and J. Mørk, *J. Lightwave Technol.*, 2017, **35**, 4247–4259.

63 J. Ren, S. Franke and S. Hughes, *Phys. Rev. X*, 2021, **11**, 041020.

64 D. A. Powell, *Phys. Rev. Appl.*, 2017, **7**, 034006.

65 R.-C. Ge, P. T. Kristensen, J. F. Young and S. Hughes, *New J. Phys.*, 2014, **16**, 113048.

66 M. Benzaouia, J. D. Joannopoulos, S. G. Johnson and A. Karalis, *Phys. Rev. Res.*, 2021, **3**, 033228.

67 H. Zhang and O. D. Miller, 2020, ARXIV, 2010.08650.

68 Z. Cao, L. Zhang, C. Y. Chan and H. C. Ong, *Opt. Lett.*, 2014, **39**, 501–504.